Effect of Internal and External Resistances on the Swelling of Droplets

Supathorn Phongikaroon
Coastal and Ocean Remote Sensing, Naval Research Laboratory, Washington, DC 20375

Richard V. Calabrese
Dept. of Chemical Engineering, University of Maryland, College Park, MD 20742

DOI 10.1002/aic.10322
Published online in Wiley InterScience (www.interscience.wiley.com).

The diffusion equation is solved, subject to a quasi-steady approximation, to determine the swelling rate of a spherical drop in an infinite medium. External convective mass transfer to the growing drop surface is accounted for as a boundary condition. Three cases are considered: the general case of finite Biot number (Bi), and the limiting cases of infinite Bi (negligible external convective resistance), and low Bi (negligible internal diffusion resistance). Analytical approximations and numerical solutions are developed and detailed results are presented. The dimensionless swelling rate is governed by a dimensionless mass driving force ($\bar{\rho}$), a dimensionless time (X_D^0), and the Biot number. The various models are compared over the range $0.001 < \bar{\rho} < 1.0$; $10^{-5} < X_D^0 < 500$; and $0.01 < Bi < \infty$ to determine when the more easily applied analytical approximations are valid, and to determine the critical Bi for which internal diffusion resistance or external convective resistance can be ignored. In these limits the simpler low Bi or infinite Bi models can be applied, respectively, in place of the finite Bi model. The results show that the analytical approximations are valid for $\bar{\rho} \leq 0.05$. Furthermore, the infinite Bi numerical solution is accurate for $Bi > 100$, whereas the low Bi solution is valid for $Bi < 1$. © 2005 American Institute of Chemical Engineers *AIChE J,* 51: 379–391, 2005

Introduction

Over the years, many solutions to the diffusion equation during phase growth have been derived. These date back to 1924 when Rieck[1] offered particular solutions for spherical and cylindrical geometries. Huber[2] quoted Rieck's work and provided a detailed discussion of these models. Frank[3] further extended these studies and incorporated cases where both heat and moisture controlled phase growth. In addition, his work included the effect of impurities within the newly formed phase boundary, as well as the effect of two dissolved substances that diffused independently to form the new phase boundary.

Correspondence concerning this article should be addressed to S. Phongikaroon at this current address: Argonne National Laboratory-West, P.O. Box 2528, Idaho Falls, ID 83403; Email: supathorn.phongikaroon@anlw.anl.gov.

Since then, many other models for phase growth by diffusion have been constructed.[4-6] For instance, Horvay and Cahn[5] provided exact solutions for the growth of elliptical paraboloids and spheroids. Several studies involved the validation of mathematical models with experimental data,[7-9] while others have offered theories explaining observed phenomena.[10] However, because of complications such as jump boundary conditions, peculiar shapes and geometries, and the need to account for a moving boundary, diffusion problems involving phase growth still remain as an important issue in chemical process applications.

The goal of this article is to investigate the relationship between, and the relative effect of, internal diffusion and external convection, and how they determine the swelling rate of a polymer or other material. Another motivation is to determine the criteria for which internal or external resistance can be

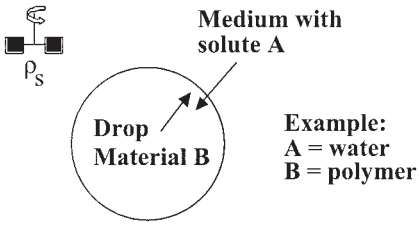

Figure 1. Liquid drop of radius *R*(*t*) in an agitated liquid medium.

neglected. The approach is to solve the transient diffusion equation for the radially symmetric swelling of a drop suspended in an infinite medium. The role of convection across the external surface boundary layer is specified as a boundary condition on the internal diffusion equation. A quasi-steady method is used to account for the moving boundary at the drop surface. Three cases are considered: the general case of finite Biot number (Bi), and the limiting cases of infinite Bi and low Bi. Both analytical approximations and numerical solutions are developed. The various cases and solutions are analyzed and compared to show their range of applicability and to determine the critical conditions at which internal diffusion or external convection can be ignored.

Model Assumptions and Constraints

Diffusion can be generally described by two classical frames of reference, molar or mass. In this study, we use the mass frame of reference for the following reasons. Consider the uptake of a solute A from the surrounding medium by a drop containing solvent B, as shown in Figure 1. A typical example is a coating material consisting of solubilized polyurethane droplets suspended in an aqueous solution.[11,12] The molecular weight of the drop material (such as B = polyurethane) and the solute (such as A = water) can be quite different so, as the drop swells, its total molar concentration will change both temporally and spatially. On the other hand, the pure component densities of the solvent and solute are often quite similar, so the total mass density within the drop remains nearly constant during swelling, facilitating the use of the mass frame of reference.

It is assumed that the drop material is insoluble in the surrounding medium and that the only component of the medium that is soluble in the drop material is solute A. For the drop phase, the differential mass balance for species A can be written as

$$\frac{\partial \rho_A}{\partial t} + \nabla \cdot \mathbf{n_A} = 0 \tag{1}$$

where ρ_A is the mass density of species A (ρ_B is the mass density of species B) and $\mathbf{n_A}$ is the mass flux of species A ($\mathbf{n_B}$ is the mass flux of species B). In the mass frame, Fick's first law of diffusion for $\mathbf{n_A}$ is given by

$$\mathbf{n_A} = w_A(\mathbf{n_A} + \mathbf{n_B}) - \rho D_{AB} \nabla w_A \tag{2}$$

where w_A is the mass fraction of A, D_{AB} is the diffusion coefficient, and ρ is the total mass density of the drop solution. It is assumed here that D_{AB} is constant. If both liquids have similar density, then $\rho = \rho_A + \rho_B$ is constant and the swelling process occurs under conditions of equimass counter-diffusion ($\mathbf{n_A} + \mathbf{n_B} = 0$). With these assumptions Eq. 2 simplifies to

$$\mathbf{n_A} = -\rho D_{AB} \nabla w_A = -D_{AB} \nabla \rho_A \tag{3}$$

Because of symmetry the flux into the drop is purely radial and the mass concentration of A depends only on time t and radial position r; that is, $\rho_A = \rho_A(r, t)$.

In addition to the aforementioned assumptions, the models developed below are subject to the constraint that the drop grows slowly compared to the time required for the density profile of solute A to fully develop inside the drop. With this later assumption, the diffusion equation can be solved for a drop of constant radius and a quasi-steady-state technique can then be applied to determine the growth or swelling rate.

The rate of mass transfer to the drop is governed by an internal resistance, arising from solute diffusion within the drop, and an external resistance, arising from convective transport from the bulk medium to the drop surface. Central to the modeling approach is the idea that the swelling rate can be modeled by specifying the convective transport rate of solute to the growing drop surface as a boundary condition on Eq. 1, which describes the internal diffusion. For the general case, the convective transport rate across the external surface boundary layer is equal to the diffusive flux into the drop. Dimensional analysis of the surface boundary condition yields the Biot number (Bi), which describes the ratio of the convective (external) to diffusive (internal) resistance

$$\mathrm{Bi} = \frac{\alpha k R_0}{D_{AB}} \tag{4}$$

where α is the partition coefficient; k is the convective mass transfer coefficient, which is assumed to be constant for reasons discussed below; and the initial drop radius R_0 is the characteristic length scale.

For $\mathrm{Bi} \gg 1$, diffusion is slow relative to convection and the internal resistance controls. Because the external resistance is negligible, the solute concentration on the external drop surface approaches the bulk value in the surrounding medium, thereby simplifying the surface boundary condition imposed on Eq. 1. This will be referred to as the *Infinite Bi Case*.

For $\mathrm{Bi} \ll 1$, diffusion is fast relative to convection and the external resistance controls. The mass concentration gradient within the drop is small and ρ_A can be approximated as a spatially uniform function of time [$\rho_A \approx \rho_A(t)$ only]. Because the internal resistance can be neglected, Eq. 1 can be replaced by a first-order (in time) lumped parameter model. This will be referred to as the *Low Bi Case*.

For intermediate values of Bi, both internal diffusion and external convection must be modeled and Eq. 1 must be solved without further simplification. This will be referred to as the *Finite Bi Case*. Because the infinite and finite Bi models require the solution of Eq. 1 they will be discussed together, followed by the lumped-parameter model for the low Bi case.

Infinite and finite Biot number cases

We begin by solving the transient diffusion equation for a drop of constant radius, and then apply the quasi-steady approximation to determine the swelling rate.

Diffusion Equation with Constant Radius. Substituting Eq. 3 into Eq. 1 with $\rho_A = \rho_A(r, t)$ only, the diffusion equation for a sphere of radius R becomes

$$\frac{\partial \rho_A(r, t)}{\partial t} = \frac{D_{AB}}{r^2}\frac{\partial}{\partial r}\left[r^2\frac{\partial \rho_A(r, t)}{\partial r}\right] \qquad 0 < r < R \quad (5)$$

If the mass concentration of solute A within the drop is initially uniform (ρ_{A0}) throughout, the initial condition is

$$\rho_A(r, t = 0) = \rho_{A0} \qquad 0 \le r \le R \quad (6)$$

Because of symmetry, the boundary condition at the center of the drop is

$$\left[\frac{\partial \rho_A(r, t)}{\partial r}\right]_{r=0} = 0 \qquad t > 0 \quad (7)$$

The drop is suspended in a well-mixed infinite medium. In the bulk of this medium (that is, except close to the drop's surface), the mass concentration of solute A remains constant and is equal to ρ_S. The solubility of A in the drop phase is ρ_{AS}, and swelling occurs for $\rho_{AS} > \rho_{A0}$. Solute phase equilibrium is defined by constant partition coefficient α, where

$$\alpha = \frac{\rho_S}{\rho_{AS}} \quad (8)$$

We first consider the infinite Bi case. Because external convective resistance is negligible, the concentration of A on the drop's external surface approaches ρ_S, so the boundary condition at the drop's internal surface becomes

$$\rho_A(r = R, t) = \rho_{AS} \qquad t > 0 \quad (9)$$

Equations 5, 6, 7, and 9 can be solved by separation of variables. The solution is well known[13] and is given by

$$\frac{\rho_A(r, t) - \rho_{AS}}{\rho_{A0} - \rho_{AS}} = 2\sum_{n=1}^{\infty}\frac{(-1)^{n+1}}{n\pi(r/R)}\exp\left(-n^2\pi^2\frac{Dt}{R^2}\right)\sin\left(n\pi\frac{r}{R}\right) \qquad (\mathrm{Bi} \to \infty) \quad (10)$$

For the case of finite Bi, the convective resistance to mass transfer at the drop's surface must be specified in the surface boundary condition, which becomes

$$-D_{AB}\left.\frac{\partial \rho_A(r, t)}{\partial r}\right|_{r=R} = \alpha k[\rho_A(r, t)|_{r=R} - \rho_{AS}] \qquad t > 0 \quad (11)$$

Using separation of variables, the solution to Eqs. 5, 6, 7, and 11 is

$$\frac{\rho_A(r, t) - \rho_{AS}}{\rho_{A0} - \rho_{AS}} = 2\sum_{n=1}^{\infty}\frac{\sin\lambda_n - \lambda_n\cos\lambda_n}{\lambda_n(\lambda_n - \sin\lambda_n\cos\lambda_n)(r/R)} \times \exp\left(-\lambda_n^2\frac{Dt}{R^2}\right)\sin\left(\lambda_n\frac{r}{R}\right) \qquad (\text{finite Bi}) \quad (12)$$

where the eigenvalues λ_n are the roots of

$$1 - \lambda_n\cot\lambda_n = \frac{\alpha kR}{D_{AB}} \quad (13)$$

where the dimensionless grouping of variables on the right-hand side is the Biot number for arbitrary R.

The mass rate of solute A into the drop can be obtained from either Eq. 10 or Eq. 12 according to

$$\dot{M}_A = -4\pi R^2 D_{AB}\left(\frac{\partial \rho_A}{\partial r}\right)_{r=R} \quad (14)$$

where $\dot{M}_A$ in Eq. 14 is positive because the flux of A is negative (in the "minus r" direction).

Quasi-Steady Approximation for Drop Growth. If it is assumed that the radius of the drop grows slowly compared to the time that it takes for the concentration profile, described by Eq. 10 or Eq. 12 to "set up" inside the drop, then a quasi-steady-state approximation can be applied to estimate the swelling rate. Subject to this restriction, the previously assumed constant drop radius in Eqs. 10, 12, 13, and 14 can be replaced by $R(t)$, and the mass rate of A into the drop can be equated to its growth rate, yielding

$$-4\pi R^2 D_{AB}\left[\frac{\partial \rho_A(r, t)}{\partial r}\right]_{r=R} = \frac{d}{dt}\left(\frac{4}{3}\pi R^3\rho\right) = 4\pi R^2\rho\left(\frac{dR}{dt}\right) \quad (15)$$

For the infinite Bi case, use of Eq. 10 yields

$$\left[\frac{\partial \rho_A(r, t)}{\partial r}\right]_{r=R} = -\frac{2}{R}(\rho_{A0} - \rho_{AS})\sum_{n=1}^{\infty}\exp\left(-n^2\pi^2\frac{D_{AB}t}{R^2}\right) \qquad (\mathrm{Bi} \to \infty) \quad (16)$$

Similarly, for the finite Bi case, use of Eq. 12 yields

$$\left(\frac{\partial \rho_A(r, t)}{\partial r}\right)_{r=R} = -\frac{2}{R}(\rho_{A0} - \rho_{AS})\sum_{n=1}^{\infty}\left[\frac{(\sin\lambda_n - \lambda_n\cos\lambda_n)^2}{\lambda_n(\lambda_n - \sin\lambda_n\cos\lambda_n)} \times \exp\left(-\lambda_n^2\frac{D_{AB}t}{R^2}\right)\right] \qquad (\text{finite Bi}) \quad (17)$$

Substituting Eq. 16 into Eq. 15 yields

$$\frac{dR}{dt} = \frac{2D_{AB}}{R}\,\bar{\rho}\sum_{n=1}^{\infty}\exp\left(-n^2\pi^2\frac{D_{AB}t}{R^2}\right) \qquad (\mathrm{Bi}\rightarrow\infty) \quad (18)$$

where the dimensionless mass driving force ($\bar{\rho}$) is defined as

$$\bar{\rho} = \frac{(\rho_{AS}-\rho_{A0})}{\rho} \quad (19)$$

Similarly, for the finite Bi case, substituting Eq. 17 into Eq. 15 yields

$$\frac{dR}{dt} = \frac{2D_{AB}}{R}\,\bar{\rho}\sum_{n=1}^{\infty}\frac{(\sin\lambda_n-\lambda_n\cos\lambda_n)^2}{\lambda_n(\lambda_n-\sin\lambda_n\cos\lambda_n)} \times\exp\left(-\lambda_n^2\frac{D_{AB}t}{R^2}\right) \qquad (\text{finite Bi}) \quad (20)$$

The initial condition on Eq. 18 or Eq. 20 is $R(t=0)=R_0$.

It is now convenient to define dimensionless variables/parameters, in addition to Bi of Eq. 4 and $\bar{\rho}$ of Eq. 19 that govern the solutions to Eqs. 18 and 20. The dimensionless drop radius is defined as $S(t)=R(t)/R_0$ and the dimensionless swelling time is defined as

$$X_D^0 = D_{AB}t/R_0^2 \quad (21)$$

Equations 18 and 20 must be integrated numerically to obtain $R(t)$ except for the special case for which $R(t=\infty)$ is not much greater than R_0. With this assumption, an analytical approximation can be achieved by replacing R with R_0 on the right-hand side of Eqs. 18 and 20. This approximate solution for the infinite Bi case is

$$S = \left\{1+\frac{4}{\pi^2}\,\bar{\rho}\sum_{n=1}^{K}\frac{1}{n^2}\left[1-\exp(-n^2\pi^2X_D^0)\right]\right\}^{1/2} \qquad (\mathrm{Bi}\rightarrow\infty) \quad (22)$$

Similarly, the approximate solution for the finite Bi case is

$$S = \left\{1+4\bar{\rho}\sum_{n=1}^{K}\frac{(\sin\lambda_n-\lambda_n\cos\lambda_n)^2}{\lambda_n^3(\lambda_n-\sin\lambda_n\cos\lambda_n)} \times\left[1-\exp(-\lambda_n^2X_D^0)\right]\right\}^{1/2} \qquad (\text{finite Bi}) \quad (23)$$

For the general case Eqs. 18 and 20 are solved numerically with $S(X_D^0=0)=1$, in the following dimensionless form:

$$\frac{dS}{dX_D^0} = \frac{2}{S}\,\bar{\rho}\sum_{n=1}^{K}\exp\left(-n^2\pi^2\frac{X_D^0}{S^2}\right) \qquad (\mathrm{Bi}\rightarrow\infty) \quad (24)$$

and

$$\frac{dS}{dX_D^0} = \frac{2}{S}\,\bar{\rho}\sum_{n=1}^{K}\frac{(\sin\lambda_n-\lambda_n\cos\lambda_n)^2}{\lambda_n(\lambda_n-\sin\lambda_n\cos\lambda_n)} \times\exp\left(-\lambda_n^2\frac{X_D^0}{S^2}\right) \qquad (\text{finite Bi}) \quad (25)$$

where the eigenvalues are the roots of

$$1-\lambda_n\cot\lambda_n = \mathrm{Bi}\,S \quad (26)$$

Low Biot number case—negligible internal resistance

If resistance to mass transfer by diffusion within the drop is negligible compared to that for external convection to its surface, the mass concentration of A in the drop becomes spatially uniform; that is, $\rho_A=\rho_A(t)$ only. The flux of A to the drop's surface is still given by the right-hand side of Eq. 11 but a lumped-parameter approach can be used. The species mass balance on the drop yields[13]

$$\frac{d}{dt}(V\rho_A) = -A\alpha k(\rho_A-\rho_{AS}) \quad (27)$$

where V and A are the volume and surface area of the spherical drop, respectively. Consistent with the quasi-steady approximation, we assume at this point that the drop radius is constant. Then the solution to Eq. 27 subject to the initial condition $\rho_A(t=0)=\rho_{A0}$, is

$$\frac{\rho_A(t)-\rho_{AS}}{\rho_{A0}-\rho_{AS}} = \exp\left(-\frac{3\alpha kt}{R}\right) \qquad (\mathrm{Bi}\rightarrow 0) \quad (28)$$

The quasi-steady approximation can be applied to determine drop growth by writing an overall mass balance on a drop of radius $R(t)$ and noting that the mass concentration of A is internally uniform.

$$\frac{d}{dt}\left(\frac{4}{3}\pi R^3\rho\right) = -4\pi R^2\alpha k[\rho_A(t)-\rho_{AS}] \qquad (\mathrm{Bi}\rightarrow 0) \quad (29)$$

Substituting Eq. 28 into Eq. 29 yields

$$\frac{dR}{dt} = \alpha k\bar{\rho}\exp\left(-\frac{3kt}{R}\right) \qquad (\mathrm{Bi}\rightarrow 0) \quad (30)$$

The initial condition is $R(t=0)=R_0$. Equation 30 must be integrated numerically to obtain $R(t)$ except for the special case for which $R(t=\infty)$ is not much greater than R_0. With this assumption, an analytical approximation can be achieved by replacing R with R_0 on the right-hand side of Eq. 30. This approximate solution is

$$S = 1 + \frac{\bar{\rho}}{3}\left[1 - \exp(-X_C^0)\right] \qquad (\mathrm{Bi} \rightarrow 0) \qquad (31)$$

$S = R(t)/R_0$ and $\bar{\rho}$ (Eq. 19) are defined as before, but the dimensionless time is given by

$$X_C^0 = 3\alpha k t/R_0 \qquad (\mathrm{Bi} \rightarrow 0) \qquad (32)$$

For the general case, Eq. 29 is solved numerically, with $S(X_C^0 = 0) = 1$, in the following form

$$\frac{dS}{dX_C^0} = \bar{\rho}\exp\left(-\frac{X_C^0}{S}\right) \qquad (\mathrm{Bi} \rightarrow 0) \qquad (33)$$

The droplet growth rates for the three cases can be compared directly, given that

$$X_C^0 = 3X_D^0\mathrm{Bi} \qquad (34)$$

Bi and X_D^0 are defined by Eqs. 4 and 21, respectively.

Numerical Methods

Implicit methods are preferred for stiff equations such as Eqs. 22, 23, and 33 to avoid stability issues associated with more popular explicit schemes. There are two possible choices: (1) functional iteration to convergence or (2) Newton iteration. The former is computationally intensive, requiring very small time steps to achieve convergence. Thus, the Newton iteration method is preferred because of its lower sensitivity to step size.

In this work, the Adams–Moulton two-point formula,[14] also known as the "Implicit Trapezoidal Method," is used to solve Eqs. 22, 23, and 33. To numerically approximate the solution of the initial-value problem

$$S' = f(X, S) \qquad a \le X \le b \qquad S(a) = S_0 \qquad (35)$$

the domain $[a, b]$ is divided into $(N + 1)$ evenly spaced intervals. The implicit trapezoidal method approximates an intermediate variable x to S at the $(N + 1)$ values of X,

$$x_0 = S_0$$

$$x_{i+1} = x_i + \frac{h}{2}\left[f(X_{i+1}, x_{i+1}) + f(X_i, x_i)\right] \qquad 0 \le i \le N - 1 \qquad (36)$$

where the step size (h) is defined as $h = (b - a)/N$. x_{i+1} is calculated using Newton's method. $x = x_{i+1}$ can be determined from the solution to

$$G(x) = x - x_i - \frac{h}{2}\left[f(X_{i+1}, x) + f(X_i, x_i)\right] \qquad (37)$$

after X_i, X_{i+1}, and x_i are known. To obtain this approximate solution, $x_{i+1}^{(0)}$ is set equal to x_i. $x_{i+1}^{(j)}$ can then be generated by applying Newton's method to Eq. 37

$$x_{i+1}^{(j)} = x_{i+1}^{(j-1)} - \frac{G(x_{i+1}^{j-1})}{dG(x_{i+1}^{j-1})} \qquad (38)$$

where

$$dG(x) = 1 - \frac{h}{2}\frac{\partial}{\partial x}f(X_{i+1}, x) \qquad (39)$$

Several iterations of Eq. 38 are required until $\left| x_{i+1}^{(j)} - x_{i+1}^{(j-1)} \right|$ is less than the specified tolerance.

For the infinite Bi case, the partial derivative of Eq. 22 is

$$\frac{\partial}{\partial S}\left(\frac{dS}{dX_D^0}\right) = -\frac{2}{S^2}\bar{\rho}\sum_{n=1}^{K}\left[\exp\left(-n^2\pi^2\frac{X_D^0}{S^2}\right)\right] + \frac{4\pi^2 X_D^0}{S^4}\bar{\rho}\sum_{n=1}^{K}\left[n^2\exp\left(-n^2\pi^2\frac{X_D^0}{S^2}\right)\right] \qquad (\mathrm{Bi} \rightarrow \infty) \qquad (40)$$

Similarly, for the finite Bi case the derivative of Eq. 23 is

$$\frac{\partial}{\partial S}\left(\frac{dS}{dX_D^0}\right) = -\frac{2}{S^2}\bar{\rho}\sum_{n=1}^{K}\left[\frac{(\sin\lambda_n - \lambda_n\cos\lambda_n)^2}{\lambda_n(\lambda_n - \sin\lambda_n\cos\lambda_n)}\exp\left(-\lambda_n^2\frac{X_D^0}{S^2}\right)\right] + \frac{4X_D^0}{S^4}\bar{\rho}\sum_{n=1}^{K}\left[\frac{\lambda_n(\sin\lambda_n - \lambda_n\cos\lambda_n)^2}{(\lambda_n - \sin\lambda_n\cos\lambda_n)} \times \exp\left(-\lambda_n^2\frac{X_D^0}{S^2}\right)\right] \qquad (\text{finite Bi}) \qquad (41)$$

For the low Bi case, the derivative of Eq. 33 is

$$\frac{\partial}{\partial S}\left(\frac{dS}{dX_C^0}\right) = \frac{3\bar{\rho}X_C^0}{S^2}\exp\left(-\frac{3X_C^0}{S}\right) \qquad (\mathrm{Bi} \rightarrow 0) \qquad (42)$$

Computational Procedures

All calculations were performed on a desktop PC. The numerical scheme was implemented within the commercial software package *Matlab*. For the finite and infinite Bi cases, both the numerically solved equations and analytical approximations contain summations with an infinite number of terms. These were approximated using the first ten eigenvalues ($K = 10$). This choice will be justified below. Results for all cases and solutions were generated for the following values of the dimensionless mass driving force: $\bar{\rho} = 0.001$, 0.005, 0.01, 0.05, 0.08, 0.1, 0.3, 0.5, 0.8, and 1.0. The appropriate interval of dimensionless time X_D^0 depended on the case and parameter set (values of Bi and $\bar{\rho}$) under consideration, and varied from 10^{-5} to 500.

Analytical Approximations. For the finite Bi case, results were generated for six different Biot numbers (Bi = 0.01, 0.1, 1, 10, 100, and 1000). For the low Bi case, Eq. 34 is used with

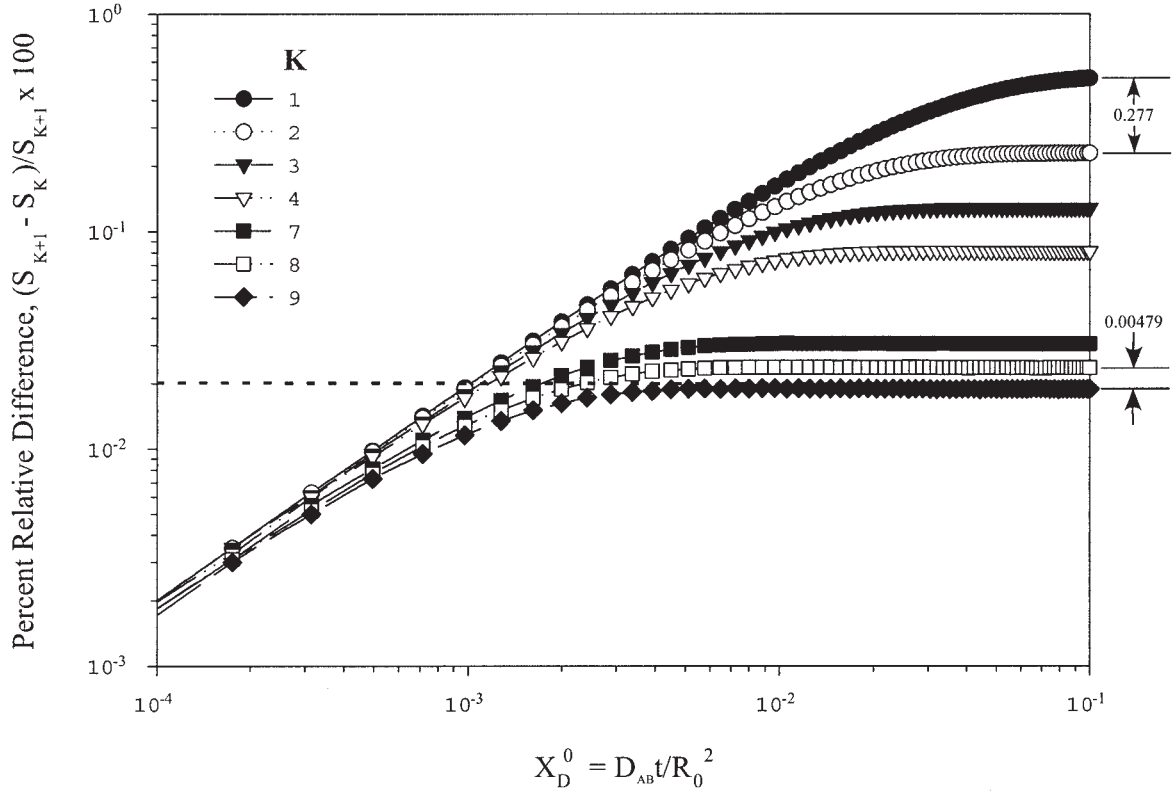

Figure 2. Percentage relative difference (PRD) vs. X_D^0 showing the effect of *K* on the resulting solution at $\bar{\rho} = 0.1$ and Bi = 0.1.

The dashed line marks the targeted acceptance criterion for this study.

Eq. 31 and the solution depends on the product of X_D^0 and Bi. Only solutions for Bi = 0.01 to 1.0 were generated.

Numerical Solutions. In the solution algorithm the absolute tolerance on *S* was set to 10^{-8}. The number of time steps *N* varied from 10,000 to 40,000 depending on the X_D^0 interval of interest. For high values of X_D^0, large values of *N* are needed to avoid error propagation. For the finite Bi case, results were generated for five different Biot numbers (Bi = 0.1, 1, 10, 100, and 1000). For this particular case, *N* depends on Bi as well. Thus, as Bi increased, *N* was increased to reduce error propa-

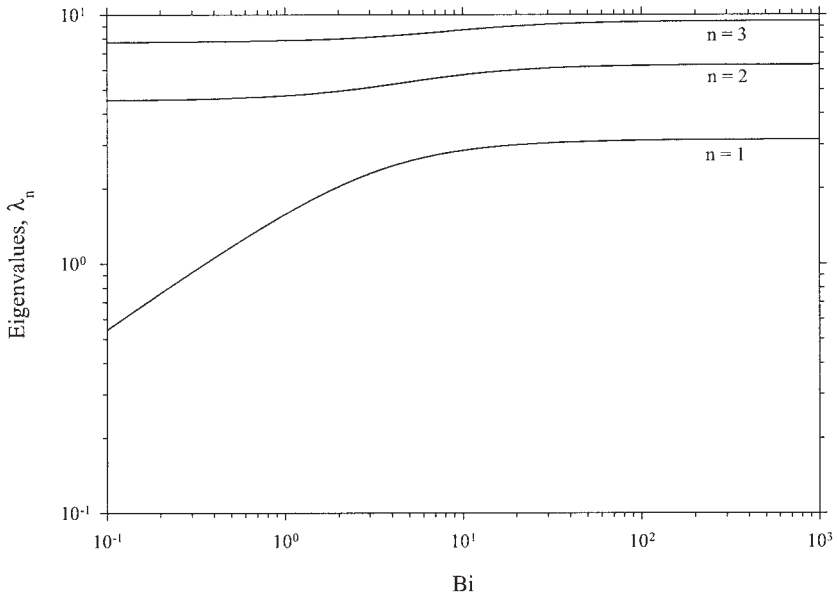

Figure 3. The first three eigenvalues for the finite Bi case.

gation. For the low Bi case, the numerical results were generated for Bi = 0.01 to 10.

Eigenvalues and infinite summations

In principle, the equations that describe the infinite Bi and finite Bi cases require the evaluation of an infinite number of eigenvalues λ_n. In practice, we minimize the number of eigenvalues (λ_1 to λ_K) that must be retained to accurately approximate the infinite summations. The largest number of terms is required at small times ($X_D^0 \sim 0.1$). To obtain an appropriate value of K, we calculated the percentage relative difference, defined as

$$\text{PRD} = 100 \times \frac{S_{K+1} - S_K}{S_{K+1}} \tag{43}$$

over the range from $10^{-4} < X_D^0 < 10^{-1}$, for the numerical solution to the finite Bi case. S_K represents the dimensionless radius S, calculated using the first K eigenvalues. The results for $\bar{\rho} = 0.1$ and Bi = 0.1 are shown in Figure 2. PRD decreases as K increases, as expected. At $X_D^0 = 0.1$ the reduction in PRD between $K = 1$ and $K = 2$ is 0.277, whereas for $K = 8$–9 it is only 0.00479. Similar trends were observed for other parameter values. The dashed line at PRD = 0.02 on Figure 2 is the targeted acceptance criterion. Thus, $K = 10$ was selected as the required number of terms for the evaluation of all summations in this work.

Figure 3 shows the first three eigenvalues as a function of Bi as evaluated from Eq. 4 with $R = R_0$ or Eq. 26 with $S = 1$. It is seen that except for λ_1, the values of λ_n are relatively insensitive to Bi, so the $K = 10$ criterion should be acceptable for all Bi > 0.1.

Results and Discussion

Comparison of analytical approximations and numerical solutions

The analytical approximations and numerical solutions are compared using results from the finite Bi and infinite Bi cases. Figures 4A–4C show the dimensionless drop radius (S) vs. dimensionless time (X_D^0), with $\bar{\rho}$ as a parameter, for the infinite Bi case. For $0.001 \leq \bar{\rho} \leq 0.05$, there is good agreement between the analytical and the numerical results. For $\bar{\rho} > 0.05$ there are discrepancies, particularly at high values of X_D^0. Furthermore, the separation point occurs at shorter times as $\bar{\rho}$ becomes larger. This is consistent with the expectation that as $\bar{\rho}$ increases, the degree of swelling increases, thereby invalidating the small growth assumption inherent in the analytical approximations. The numerical results show quantitatively the degree to which $\bar{\rho}$ influences the extent of swelling. Table 1 provides the asymptotic or maximum radius ($S_{\max}$) as a function of $\bar{\rho}$ for the numerical solutions.

To determine the domain of validity of the analytical approximations, the percentage relative deviation, defined as $(S_n - S_a)/(S_n - 1) \times 100$, where subscripts n and a stand for numerical and analytical, respectively, was calculated. It is plotted against dimensionless time X_D^0 in Figure 5. Important details for $0.007 < X_D^0 < 0.05$ are provided in the insert. As discussed, the relative deviation increases as both $\bar{\rho}$ and X_D^0 increase. The figure can be used to determine the acceptable

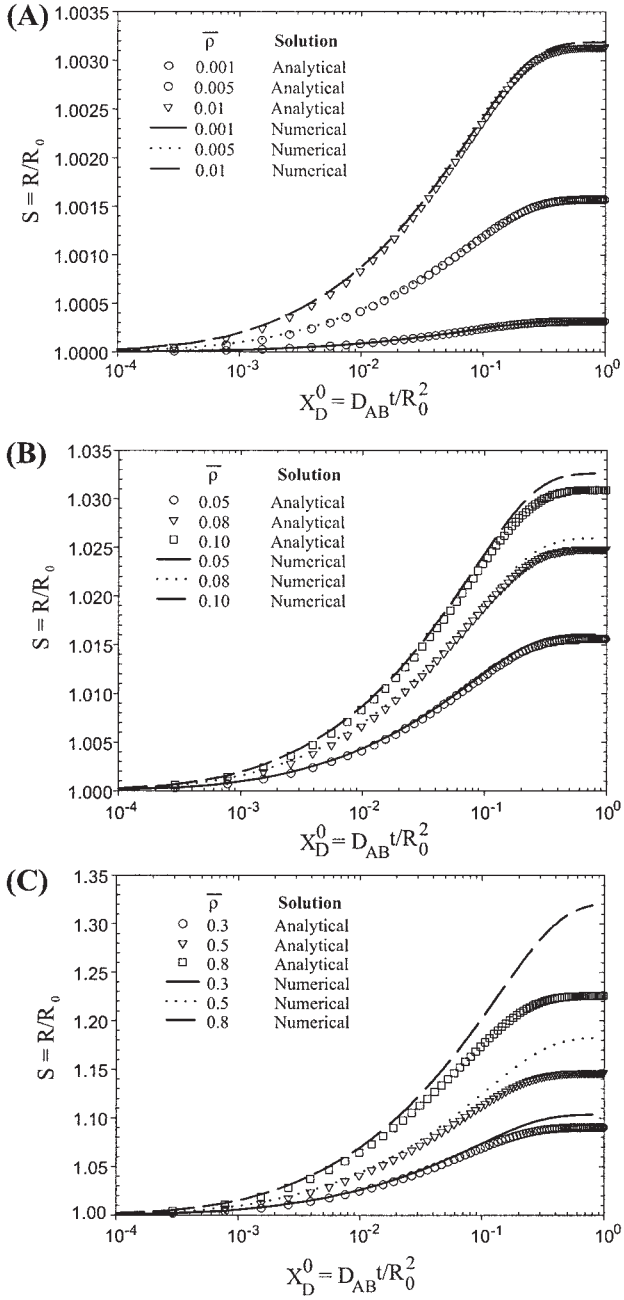

Figure 4. (A)–(C): Relative influence of $\bar{\rho}$ on S vs. X_D^0 for the infinite Bi case.

The graphs provide a comparison between the analytical approximation and numerical solution.

error. For instance, for $\bar{\rho} = 1.0$ and $X_D^0 = 0.03$, the analytical solution would yield 8% relative deviation from the numerical solution. To use the analytical model to approximate the growth rate, with less than 3% relative deviation, limits it use to $X_D^0 < 0.01$. Figure 5 can also be used together with Figure 4. For instance, if the analytical solution of Figure 4C for $\bar{\rho} = 0.8$ is to be used for $X_D^0 < 0.01$, then Figure 5 shows that the relative deviation from the numerical solution is always <4%.

Figures 6A–6C show the analytical approximations vs. numerical solutions at Bi = 0.01 for $0.001 < \bar{\rho} < 0.8$. The trends

Table 1. Effect of Bi and $\bar{\rho}$ on S_{max} of Numerical Solutions

	$S_{max} = R/R_0$						
$\bar{\rho}$/Bi	0.01	0.1	1	10	100	1000	∞
0.001	1.000334	1.000334	1.000334	1.000333	1.000322	1.000320	1.000318
0.005	1.00167	1.00167	1.00167	1.00166	1.00161	1.00159	1.00159
0.01	1.00335	1.00335	1.00335	1.00334	1.00323	1.00319	1.00318
0.05	1.0170	1.0170	1.0170	1.0169	1.0163	1.0161	1.0161
0.08	1.0274	1.0274	1.0274	1.0273	1.0263	1.0259	1.0259
0.10	1.0345	1.0345	1.0345	1.0343	1.0330	1.0325	1.0326
0.30	1.1111	1.1111	1.1111	1.1096	1.1049	1.1034	1.1033
0.50	1.1998	1.1998	1.1994	1.1951	1.1851	1.1820	1.1820
0.80	1.3621	1.3621	1.3610	1.3456	1.3232	1.3189	1.3190
1.00	1.4953	1.4956	1.4920	1.4626	1.4278	1.4170	1.4232

are similar to those for the infinite Bi case. That is, discrepancies between the analytical and numerical results occur when $\bar{\rho} > 0.05$ and occur earlier in time as $\bar{\rho}$ becomes larger. Figures 7A–C show similar plots at Bi = 0.1. A noticeable difference between the results of Figures 6 and 7 is the range on X_D^0. The range on X_D^0 at Bi = 0.01 ($1 < X_D^0 < 300$) is larger than that at Bi = 0.1 ($0.1 < X_D^0 < 30$). The range is even smaller for infinite Bi (Figure 4). This comparison indicates that, although $\bar{\rho}$ determines the maximum drop radius (S_{max}), the Biot number controls the growth rate or time to achieve S_{max}. Values of S_{max} vs. $\bar{\rho}$ with Bi as a parameter ($0.1 \leq Bi \leq 1000$), taken from the numerical solutions, are shown in Table 1. It is seen that the magnitude of Bi practically does not influence S_{max}. Percentage relative deviation plots for Bi = 0.01 and Bi = 0.1 are shown in Figures 8A and B, respectively. The trends in these plots are similar to those of Figure 5, except that finite deviations are displaced to smaller times, as discussed above. The rate of increase is also larger.

Finite Bi case: internal resistance vs. external resistance

Here, the numerical solutions for the finite Bi case are presented and compared to those for the limiting cases (Bi → 0 and Bi → ∞) to determine when the simpler limiting case models can be accurately applied. Figures 9A–9C show the relative effect of Bi on S vs. X_D^0 for $\bar{\rho}$ equal to 0.001, 0.01, and 0.1, respectively. As discussed earlier, as $\bar{\rho}$ increases S_{max} also increases, and the values of S_{max} at different Bi and $\bar{\rho}$ are listed in Table 1. Furthermore, as Bi decreases, it takes longer for a drop to reach its maximum size. For Bi < 1, decreasing Bi by an order of magnitude increases the time for the drop to grow by an order of magnitude. For Bi > 1, the influence of Bi on the growth time decreases with increasing Bi, as the infinite Bi limit is approached. The numerical solution for the infinite Bi case is shown as a solid line on Figures 9A–9C. A comparison indicates that when Bi > 100, the convective resistance can be neglected. The Bi = 100 and Bi = 1000 results lie on top of each other.

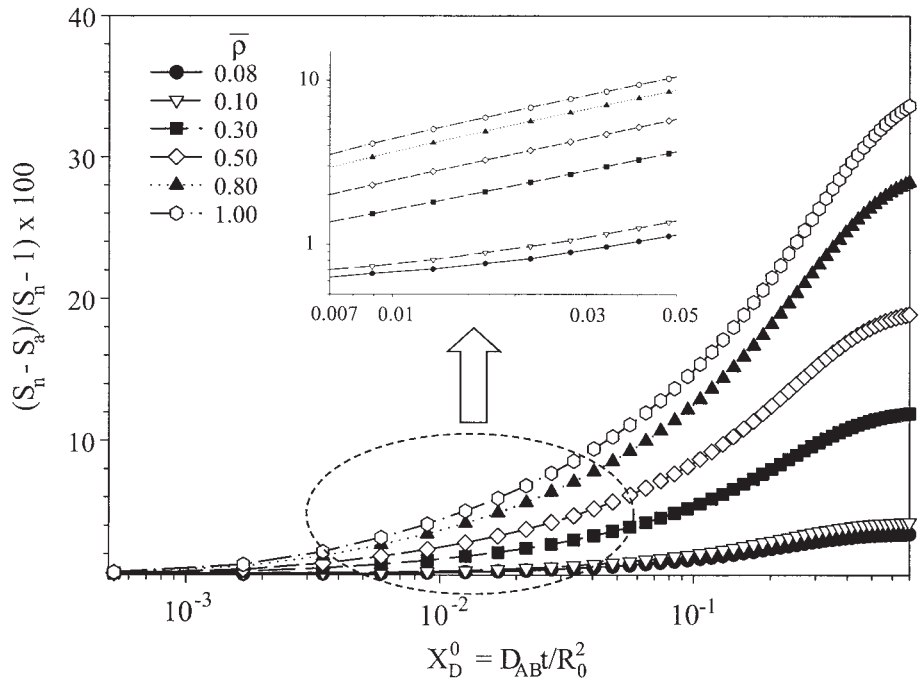

Figure 5. Percentage relative deviation vs. X_D^0 showing the domain of validity of the analytical approximation to the numerical solution for the infinite Bi case.

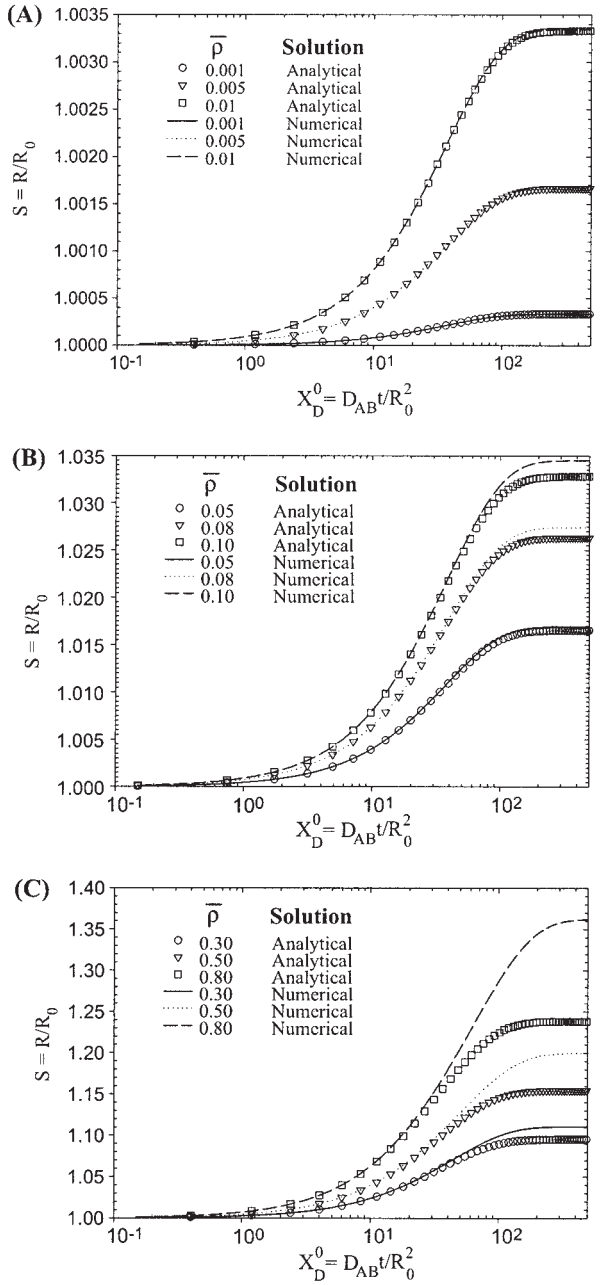

Figure 6. (A)–(C): Relative influence of $\bar{\rho}$ on S vs. X_D^0 for Bi = 0.01.

The graphs provide a comparison between the analytical approximation and numerical solution.

For the low Bi case (Bi $\rightarrow$ 0), all resistance to mass transfer lies in the external (convection) phase, so the growth rate (Eq. 30) does not contain the drop diffusivity. To obtain the criterion for neglecting internal resistance, we can manipulate the finite Bi solutions, by reference to Eq. 34 and recast them as plots of $S(X_D^0\text{Bi}, \text{Bi})$. These plots are shown for Bi $\leq$ 10 in Figures 10A–D for $\bar{\rho}$ equal to 0.001, 0.005, 0.01, and 0.05, respectively. The curves for Bi = 0.1 and Bi = 0.01 collapse to a single line independent of Bi. The Bi = 1 curve is essentially the same. This collapsed result is compared to the low Bi numerical solution of Eq. 33 (solid line) in Figure 10A. For $\bar{\rho} \leq 0.05$ the analytical solution of Eq. 31 is identical to the solid line, and can be used to determine the radius of the drop. Figures 11A–11F are similar plots of numerical solutions, but at high values of $\bar{\rho}$. As before, as $\bar{\rho}$ increases, S increases accordingly. It can be concluded from Figures 10 and 11 that internal diffusion resistance can be neglected for Bi < 1, where the solution for the low Bi case can be accurately applied.

Effect of Bi on S_{max}

Although of no practical significance, it can be seen from Figures 9A–9C and Table 1 that the values of $S_{\max}$ decrease

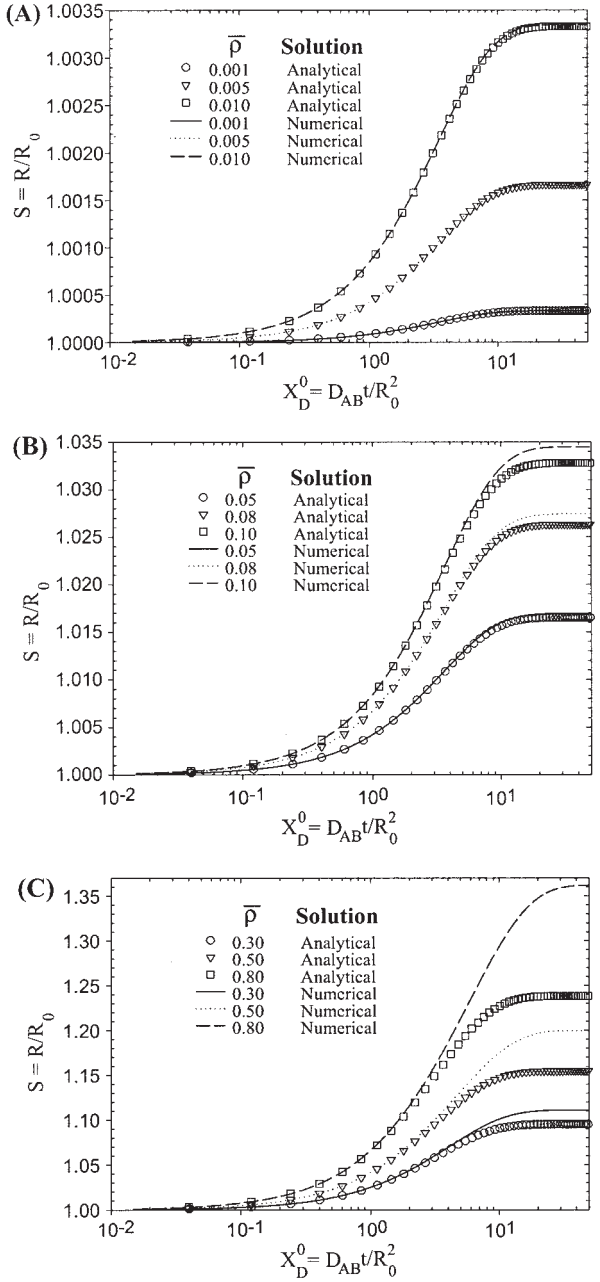

Figure 7. (A)–(C): Relative influence of $\bar{\rho}$ on S vs. X_D^0 for Bi = 0.1.

The graphs provide a comparison between the analytical approximation and numerical solution.

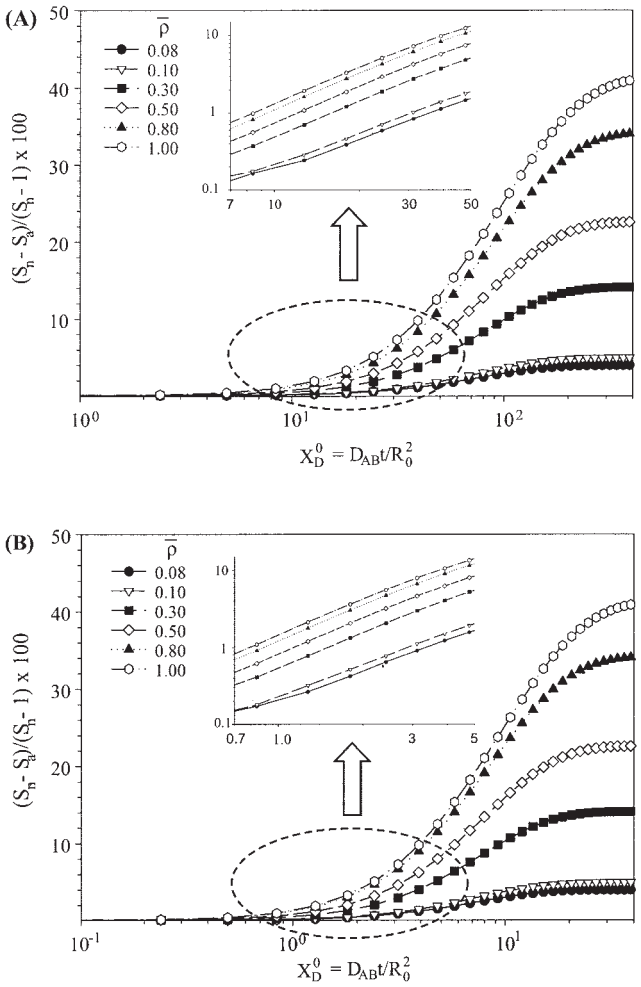

Figure 8. (A)–(B): Percentage relative deviation vs. X_D^0 showing the domain of validity of the analytical approximations to the numerical solutions for (A) Bi = 0.01 and (B) Bi = 0.1.

slightly as Bi increases. This decrease is not the result of numerical solution errors and can be explained as follows. At high Biot number, the mass concentration gradient within the drop is large and the concentration gradient across the external boundary layer on the drop surface is small. Therefore, the species *A* entering the drop at its surface slowly diffuses and distributes, causing the drop to grow slightly smaller than at low Biot number. At low Bi the mass concentration gradient within the drop is small and the concentration gradient across the external boundary layer on the drop surface is large. Therefore, the species *A* entering the drop at its surface rapidly diffuses and distributes, enhancing its growth. This argument can be confirmed mathematically by comparing the analytical solutions for the low and infinite Bi cases. When $X_D^0 \to \infty$ (this implies that $X_C^0 \to \infty$ according to Eq. 34), the ratio of Eq. 22 to Eq. 31 becomes

$$\frac{S_{\max \text{ at Bi}\gg 1}}{S_{\max \text{ at Bi}\ll 1}} = \frac{\left(1 + \dfrac{4\bar{\rho}}{\pi^2}\displaystyle\sum_{n=1}^{\infty}\frac{1}{n^2}\right)^{1/2}}{1 + \dfrac{\bar{\rho}}{3}} = \frac{\left(1 + \dfrac{2\bar{\rho}}{3}\right)^{1/2}}{1 + \dfrac{\bar{\rho}}{3}} \qquad (44)$$

where

$$\sum_{n=1}^{\infty}\frac{1}{n^2} = \frac{\pi^2}{6}$$

Thus

$$\frac{S_{\max \text{ at Bi}\gg 1}}{S_{\max \text{ at Bi}\ll 1}} < 1$$

so $S_{\max}$ at high Bi will be lower than that at low Bi.

Constant mass-transfer coefficient assumption

In the approach used here, it is assumed that the mass-transfer coefficient is constant during particle growth. Based on the results of Table 1, the use of the initial particle size to determine k is certainly valid for $\bar{\rho} \leq 0.1$. At high $\bar{\rho}$ the drop size can change by as much as 50%. However, there are many situations where the use of a constant mass-transfer coefficient is not overly restrictive, even at high $\bar{\rho}$.

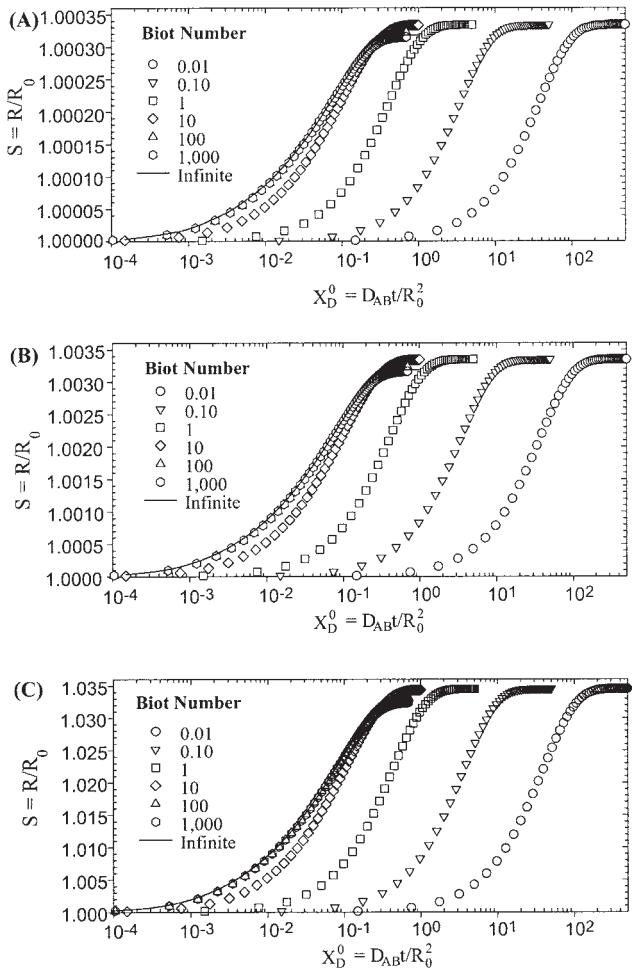

Figure 9. (A)–(C): Relative influence of Bi on the numerical solutions for *S* vs. X_D^0 for $\bar{\rho}$ equal to (A) 0.001, (B) 0.01, and (C) 0.1.

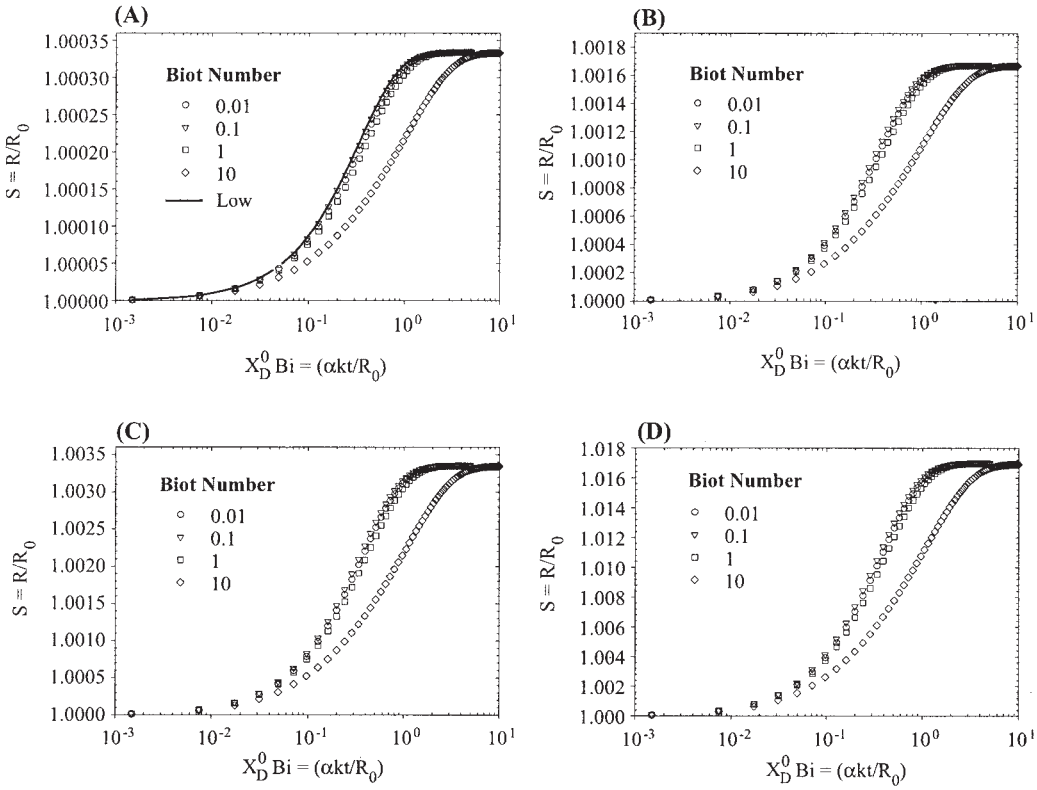

Figure 10. (A)–(D): Relative influence of Bi on numerical solutions for S vs. X_D^0Bi for $\bar{\rho}$ equal to (A) 0.001, (B) 0.005, (C) 0.01, and (D) 0.05.

Correlations for mass transfer coefficients for single spheres are usually of the Froessling type, and of the form

$$\mathrm{Sh} = \frac{kd}{D_{AB}} = 2 + a\,\mathrm{Re}^b\mathrm{Sc}^c \tag{45}$$

where Sh is the Sherwood number, d is the particle diameter, Re is an appropriately defined Reynolds number, and Sc is the Schmidt number. a, b, and c are empirical constants with $c \approx 1/3$. For low Reynolds number, k is inversely proportional to particle size so the assumption of constant k is not valid at high $\bar{\rho}$. However, drop swelling processes often occur under highly agitated conditions at high Reynolds number, so the second term on the righthand side of Eq. 45 is large compared to 2. For the classical correlation, the Reynolds number is based on the slip velocity and $b = 1/2$. Then $k \sim d^{-1/2}$, thereby extending the range of $\bar{\rho}$ for which the constant mass-transfer coefficient assumption is valid.

Under turbulent conditions, it is often the case that the drop size is small compared to the turbulent macroscale and large compared to Kolmogorov microscale. Mass transfer is controlled by inertial subrange eddies and the characteristic velocity is proportional to $\varepsilon^{1/3}d^{1/3}$, where ε is the local energy dissipation rate. The appropriate Reynolds number becomes $\mathrm{Re} = \varepsilon^{1/3}d^{4/3}/\nu$, where ν is the kinematic viscosity of the continuous phase. A recommended correlation for solids suspended in stirred tanks[15] gives $b = 0.62$. Then $k \sim d^{-0.17}$, so even for $\bar{\rho} = 1.0$ ($S_{\max} < 1.5$), k would not vary by >7%. Other stirred tank correlations show no dependency on particle size and use the impeller diameter as the characteristic length scale. It is apparent that there are many situations where the assumption of constant mass-transfer coefficient is not overly restrictive. Because $S_{\max}$ is essentially independent of Bi, it is known a priori for a given $\bar{\rho}$. Therefore, k can be based on the average drop size during the growth process.

Summary

The results of this study show that the drop radius increases with $\bar{\rho}$, but the asymptotic value $S_{\max}$ is almost independent of Bi. However, the time required to reach $S_{\max}$ increases with decreasing Bi, particularly at low Bi. That is, Bi is the parameter that controls the growth rate, whereas $\bar{\rho}$ is the parameter that controls the ultimate drop size. Values of $S_{\max}$, obtained from the numerical solutions, for infinite and finite Bi cases are given in Table 1. For all cases the analytical approximations to the numerical solutions are valid for $\bar{\rho} \leq 0.05$. For $\bar{\rho} > 0.05$ plots of the percentage relative deviation are given in Figures 5 and 8 to show the applicable range of the analytical solutions. Beyond these ranges, the numerical solutions are recommended. For all $\bar{\rho}$ and X_D^0, the low Biot number numerical solution is valid for Bi $\leq$1, and the infinite Biot number numerical solution is valid for Bi $\geq$ 100. For a given $\bar{\rho}$, the value of $S_{\max}$ decreases slightly with increasing Bi. This observation is not a result of numerical error and can be explained both physically and mathematically.

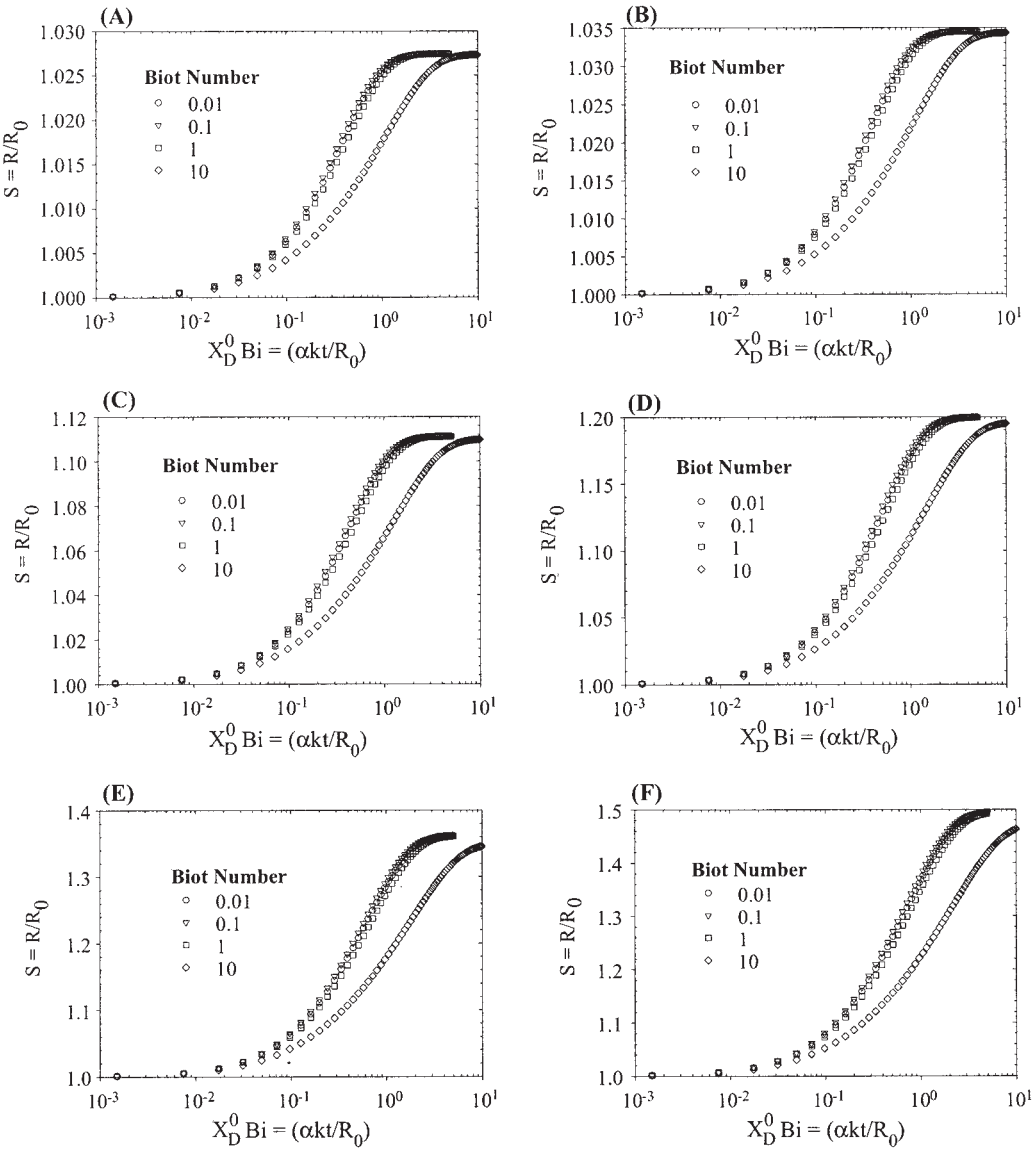

Figure 11. (A)–(F): Relative influence of Bi on numerical solutions for S vs. X_D^0Bi for $\bar{\rho}$ equal to (A) 0.08, (B) 0.1, (C) 0.3, (D) 0.5, (E) 0.8, and (F) 1.0.

Acknowledgments

This work was begun while S.P. was a doctoral candidate at the University of Maryland and completed while he was a Postdoctoral Associate at the Naval Research Laboratory (NRL). Both authors acknowledge financial support from the Zeneca Strategic Research Fund (SRF No. 269) and the University of Maryland High Shear Mixing Research Program, Industrial Advisory Board. S.P. acknowledges financial support from the National Research Council Postdoctoral Associateship Program. The authors thank Dr. Keith J. Carpenter of Zeneca, and Dr. K. Peter Judd of NRL and Gregory Fike for their useful comments and suggestions.

Notation

A = surface area of a spherical drop
a = lowest end point of interval X_D
a = empirical constant, defined in Eq. 45
Bi = Biot number, defined in Eq. 4
b = highest end point of interval X_D
b, c = empirical constants, defined in Eq. 45
d = particle diameter
D_{AB} = diffusion coefficient
$G(x)$ = function, defined in Eq. 37
h = step size, defined as $h = (b - a)/N$
k = convective mass transfer coefficient
L = characteristic length
$\dot{M}_A$ = mass density flux
N = number of interval for numerical scheme
$\mathbf{n}_A$ = mass flux of species A
$\mathbf{n}_B$ = mass flux of species B
R_0 = sphere radius at stationary
R = sphere radius at $t = 0$, involve moving boundaries
r = radius vector
Re = Reynolds number
S = dimensionless growth radius, defined as $S = R/R_0$
Sc = Schmidt number
Sh = Sherwood number
t = time or processing time
V = volume of a spherical drop
w_A = mass fraction of A
X = dimensionless time variable for numerical scheme

X_D = dimensionless time, defined as $X_D = D_{AB}t/R^2$
X_C = modified dimensionless time, defined as $X_C = X_D\text{Bi}$
x = intermediate variable for numerical scheme

Greek letters

α = thermodynamic equilibrium partition coefficient
ε = local energy dissipation rate
λ_n = eigenvalues having the roots to Eq. 13
ν = kinematic viscosity of the continuous phase
ρ = overall density of the drop, defined as $\rho = \rho_A + \rho_B$
ρ_A = uniform mass density of species A per unit volume of solution at $t = 0$
ρ_{AS} = mass density of species A per unit volume of solution at the surface, defined as $\rho_S = \alpha\rho_{AS}$
ρ_S = uniform mass density of an aqueous medium
$\bar{\rho}$ = dimensionless mass driving force, defined as $\bar{\rho} = (\rho_{AS} - \rho_{A0})/\rho$

Literature Cited

1. Crank J. *The Mathematics of Diffusion*. Oxford, UK: Oxford Univ. Press; 1975.
2. Huber VA. Über das fortschreiten der schmelzgrenze in einem linearen leiter. *ZAMM.* 1939;19:1-20.
3. Frank FC. Radially symmetric phase growth controlled by diffusion. *Proc. R. Soc. London Ser. A.* 1950;201:586-599.
4. Zener G. Theory of growth of spherical precipitates from solid solution. *J. Appl. Phys.* 1949;20:950-953.
5. Horvay G, Cahn JW. Dendritic and spheroidal growth. *Acta Metall.* 1961;9:695-705.
6. Yu G, Lai YKL, Zhang W. Kinetics of transformation with nucleation and growth mechanism: Diffusion-controlled reactions. *J. Appl. Phys*. 1997;82:4270-4276.
7. Reiss H, La Mer VK. Diffusional boundary value problems involving moving boundaries, connected with the growth of colloidal particles. *J. Chem. Phys*. 1950;18:1-12.
8. Liotta V, Georgakis C, Sudol ED, El-Aasser SE. Manipulation of competitive growth for particle size control in emulsion polymerization. *Ind. Eng. Chem. Res*. 1997;36:3252-3263.
9. Fransaer JL, Penner RM. Brownian dynamics simulation of the growth of metal nanocrystal ensembles on electrode surfaces from solution. I. Instantaneous nucleation and diffusion-controlled growth. *J. Phys. Chem. B*. 1999;103:7643-7653.
10. Yaghi OM, Li G, Li H. Crystal growth of extended solids by nonaqueous gel diffusion. *Chem. Mater.* 1997;9:1074-1076.
11. Satguru R, McMahon J, Padget JC, Coogan RG. Aqueous polyurethanes—Polymer colloids with unusual colloidal, morphological, and application characteristics. *J. Coat. Technol*. 1994;66:47-55.
12. Phongikaroon S. *Drop Size Distribution for Liquid–Liquid Dispersions Produced by Rotor-Stator Mixers*. PhD Dissertation, College Park, MD: University of Maryland; 2001.
13. Middleman S. *An Introduction to Mass and Heat Transfer*. New York, NY: Wiley; 1998.
14. Burden RL, Faires JD. *Numerical Analysis*. New York, NY: Thomson Publishing Co.; 1997.
15. Atiemo-Obeng VA, Penney WR, Armenante PA. Solid-liquid mixing. In: Paul EL, Atiemo-Obeng VA, Kresta SM, eds. *Handbook of Industrial Mixing Science and Practice*. New York, NY: Wiley; 2004:543-582.

Manuscript received Dec. 1, 2003, and revision received Jun. 8, 2004.